

Structured slope errors on real x-ray mirrors: Ray-tracing versus Experiment

R. Signorato and M. Sánchez del Río

European Synchrotron Radiation Facility
BP 220, 38043 Grenoble-Cedex 9, France

ABSTRACT

Ray-tracing plays an essential role for the design of a synchrotron radiation beamline optics. Nevertheless, it can also be extremely useful during the commissioning phase of a beamline. At that moment, it is possible to include real surface figure errors in the computer simulation of the optical devices. The resulting focal spot size and photon flux values are the final targets for the experimental optimization and alignment of the optics setup. We report on extensive ray-tracing of the mirror systems of the two beamlines placed at the ESRF insertion device 12. Slope errors measured after mirror delivery are included in the calculations. It is demonstrated how slope errors with characteristic periodicity between 1 and ca. $1/20$ of the mirror length can affect the focal spot shape, size and position. In particular, they can create structures or satellites in the focal spot. The distortions from the ideal shape are generated by the polishing process itself and are intrinsic to each single mirror. Comparison between the effects of slope errors in ray-tracing using either real (measured) surfaces or numerically generated ones are also reported.

Keywords: ray-tracing, slope error, x-ray mirror, synchrotron radiation beamline, PSD, mirror metrology

1. INTRODUCTION

Ray-tracing calculations are an important tool for synchrotron beamline optical design and optimization. SHADOW¹ is the most widely used computer code, as it is freely available, very flexible and gives good estimations for the transmitted flux, energy resolution and intensity distributions. It is optimized for synchrotron radiation applications and includes accurate models for simulating x-ray sources (undulators, wigglers and dipoles) as well as mirror, grating, crystal (Bragg and Laue geometry), multilayer and single/polycapillary optics.

In a x-ray mirror system, three parameters mainly determine the intensity distribution at the focal position: the real source characteristics (geometrical size and divergence), the reflecting surface shape (spherical or aspherical) and its figure errors. It is worth to determine their respective contributions to the final image because there are technical limits to the accuracy of the mirror finish intrinsic to the mechanical polishing process. Moreover, the optical elements price increases considerably when slightly reducing their figure imperfections below certain limits.

The optical surface texture can be classified in three families²: roughness, slope errors or waviness, and figure or geometry errors. Figure (geometry) errors corresponding to deformations such as the thermal bump due to heat load or the sagging due to gravity can be easily analytically modelled and studied with ray-tracing. On the contrary, waviness and roughness can be effectively included in the computer simulation only if a good characterization of the real mirror is provided. It is well known that the rms values of slope error and roughness, as they are requested in many mirrors technical specifications, do not give the necessary information to fully predict their effects on the final image quality. For this purpose, the mirror profile obtained from metrology measurements is needed. Sometimes, the power spectral density function (PSD) is an efficient tool to understand the effect of imperfections.

Surface roughness causes wide angle scattering of the photon beam, resulting in a blur of the image and a loss of contrast at the focal point. The knowledge of the PSD for the higher spatial frequencies (shorter than 1 mm^{-1} , approximately) is sufficient to predict statistically this effect (diffractive scattering regime). In most practical cases, extremely low values of the rms roughness ($<5 \text{ \AA}$) are routinely achieved, thus limiting the intensity loss to a few

Other author information: (Send correspondence to R.S.)

R.S.: Email: signorato@esrf.fr; Telephone: +33-476 882 602; Fax: +33-476 882 707;

M.S.R.: Email: srio@esrf.fr; Telephone: +33-476 882 513; Fax: +33-476 882 160

percent of the total incoming flux. Moreover, part of the non specularly reflected photons are often scattered into the focal region illuminated when other experimental factors (finite source size, optical aberrations and lower frequency slope errors) are present.

Waviness (or slope error) imperfections produce specular deflection of the rays from their ideal path. Their spatial periods go from few parts of the mirror length to those corresponding to roughness. Waviness can always be treated within the geometrical optics model in the ray-tracing simulations. Waviness effects associated with spatial wavelengths shorter than $1/15$ of the mirror length produce a broadening of the ideal focal spot. In this paper it is shown, both experimentally and theoretically, how slope errors associated with spatial periods in the range between $1/3 - 1/4$ and about $1/15$ of the mirror length can also lead to satellite structures very close to the main focal spot. These surface imperfections (that we called structured slope errors) belong to an intersection zone between waviness and figure errors. They generate a plateau in the low frequency range of the PSD. However, it is important to stress here that the PSD cannot completely determine the reflectivity properties of the mirror, because it does not carry information on the phases of profiles. The reflecting surface profile cannot be reconstructed by knowing its PSD. Measured profiles of the mirror in the correct bandwidth window are then necessary to simulate errors in this frequency range. Hereafter we report on some extensive ray-tracing calculations concerning several mirrors whose real profiles were measured in the ESRF metrology laboratory. The effect of the structured slope errors is evident both in the experimental data and in the simulations.

The calculations presented in this paper point out the importance of computer modeling simulations while commissioning the beamline. Although analytical studies and also ray-tracing calculations performed during the optical layout design phase often give reliable values of the expected optical properties (i.e. spot size at the important points of the beamline -slit and sample positions-, estimated photon flux, energy bandpass...), it is clear that real optical devices may not be able to reproduce such figures. These numbers can generally be taken into account as a reliable indication of the best performances one can expect from the system under study. The behavior of a real optical element, affected by unavoidable manufacturing imperfections, will in general differ from its "ideal" counterpart. Thus, a careful characterization of the mirror/grating surface is important not only to verify that the technical specifications are fulfilled, but also to obtain data that, after being inserted in a ray-tracing code, will give reliable values of what can and cannot be obtained experimentally.

2. BEAMLINES AND MIRRORS DESCRIPTION

2.1. The beamlines

Two insertion devices are installed in the ESRF storage ring straight section 12 (ID12): Helios I and Helios II.³ Both are helical undulators, designed to produce extremely intense beams of polarized x-rays. Two beamlines exploit the radiation emitted by these undulators. The first, beamline ID12A,^{4,5} is dedicated to polarization dependent studies in the hard x-ray spectral range (2.3-20 keV). The second, ID12B,⁵ operates in the soft x-ray energy range from 0.5 to 1.5 keV. Both beamlines are equipped with an x-ray monochromator (a double crystal system for ID12A and a spherical grating for ID12B) and several mirrors. A decisive advantage in favor of reflective optics is their excellent polarization transfer function. The mirror systems installed in the beamlines mentioned above are the object of the studies presented in this article. All the mirrors were carefully characterized after delivery by the manufacturer in the ESRF metrology laboratory and the results were used in the commissioning phase to help in the alignment and tuning.

A vertically focusing double mirror device (VF-2M)^{6,7} is installed in ID12A beamline downstream of the fixed exit double crystal monochromator. Its two main functions are: i) it acts as a low pass filter in energy to reject (by at least 4 orders of magnitude) unwanted higher order harmonics transmitted by the monochromator, and ii) it is used to focus vertically the monochromatic beam at the sample position. The focusing of the beam is needed for many experiments requiring a high photon density at the sample location, such as x-ray magnetic circular dichroism, XPS, high resolution fluorescence spectrometry or XAS under high pressure. Besides the well known advantages offered by any double mirror system (e.g., the direction of the transmitted beam is kept unchanged, lack of transmission of unreflected or scattered photons, poor sensitivity to uncorrelated vibrations of the floor), the VF-2M design is shown to self-compensate the gravity sag.⁶ Fig. 1 presents a schematic view of the ID12A VF-2M.

Beamline ID12B is based on the DRAGON concept.^{8,9} As it operates mainly in the soft x-ray range, its active element is a spherical grating monochromator. Due to manufacturing limits and costs, only flat and spherical mirrors

are used in order to assure very good values of figure slope error and roughness. The first optical elements are a set of flat deflecting mirrors (DFM1 and DFM2), which deviate the two Helios I beams in the horizontal plane. These two mirrors are non-critical optical components and remove most of the undesirable heat load before the more sensitive focusing optics. Another set of two mirrors located very close to the DFMs is used to refocus horizontally each deflected beam in the horizontal plane (mirrors HFM1 and HFM2) onto the exit slit of the grating monochromator. The two beams are vertically focused onto the entrance slit of the grating monochromator by a single mirror (VFM). A postfocusing mirror (PFM) has recently been added after the spherical grating to improve the photon density at the sample. A schematic view of the ID12B beamline is shown in Fig. 1.

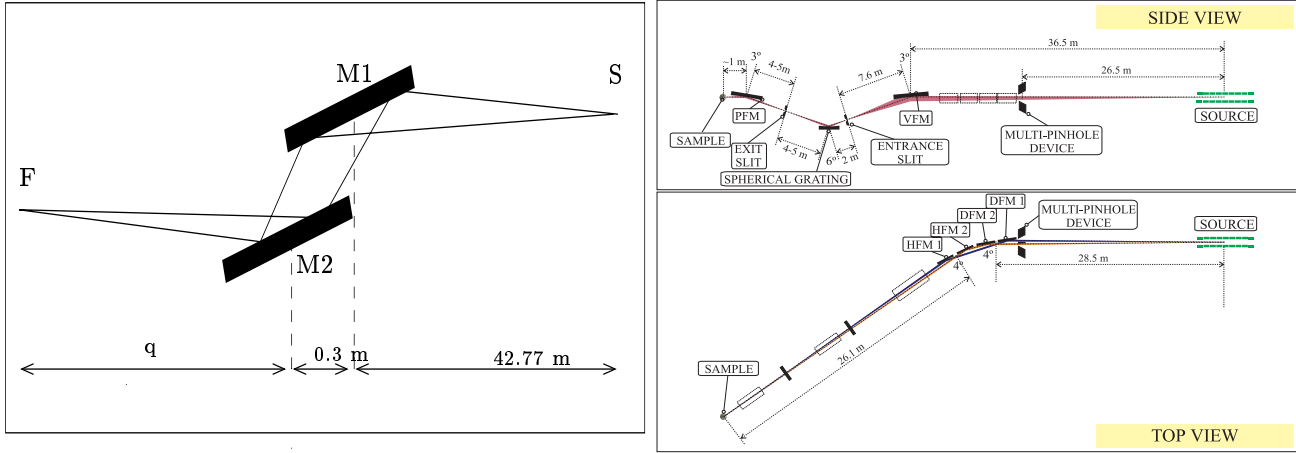


Figure 1. Left: Schematic side view of the ID12A VF-2M device (S=source, F=focal position) Right: Layout of ID12B beamline.

2.2. Mirrors Description

The ID12A VF-2M consists of two identical bendable mirrors made of bulk CVD SiC. They are mounted in an antiparallel configuration: the first mirror (M1) is facing downwards, while the second one (M2) reflects the beam upwards. The mirrors are intended to operate at grazing angles between 2 and 10 mrad. No cooling is needed because the incoming beam is monochromatic and the heat load is practically negligible. M1 and M2 were polished to an initial rather short concave radius of ca. 1 Km. To modify dynamically their curvature radius, a four-point bender has been developed in-house at the ESRF. The bender active elements are two ultra high vacuum compatible digital piezo actuators which push each mirror from its backside. It is possible, by increasing the force applied by the piezos, to obtain flat and eventually convex optical shapes. M1 and M2 were polished to a rather short concave bending radius to avoid reversing the direction of the piezo movement during the full range radius scan. The mirrors can be scanned through the whole dynamic curvature range (approx. from 1 Km concave to 1 Km convex) keeping the figure slope error below $6/7 \mu rad$ rms (as shown later).

Beamline ID12B mirrors (with the exception of the PFM, made from a fused silica substrate) are also made from thick CVD SiC substrates polished to excellent figure slope errors (see Table 1). Due to the larger grazing incidence angles (few degrees) in the soft x-ray domain, they are shorter than ID12A mirrors. This allowed to specify, and eventually obtain, better values for rms slope error. All of them have a fixed focal.

We used only one DFM and one HFM profiles in our simulations. This is justified by the following three assumptions: i) by properly adjusting the incidence angle on the DFMs and HFMs the two Helios I beams are eventually very well superimposed at the sample position ii) the DFMs, as well as the HFMs, were manufactured together on the same polishing machine: they show practically the same optical surface finish. iii) the two beams footprints on the VFM, spherical grating and PFM are very close (less than 5 mm), so one can assume that the mirror is isotropic over such a scale. The main parameters for both ID12A and ID12B mirrors are shown in table 1.

Table 1. Relevant optical parameters for the ID12A and ID12B mirrors.

ID12A	Source-M1 distance	42.77 m
	distance M1-M2	0.3 m
	distance M2-sample	7.64 m
	VF-2M geometrical magnification factor	ca. 0.2
	M1 & M2 coating	Cr, bare SiC
	M1 & M2 rms roughness	2.5 Å
	M1 & M2 dimensions (length (L), width, thickness)	600 x 40 x 12 mm ³
	Grazing angle on M1 & M2	5 mrad
Beam footprint on M1 & M2	250 mm = L/2.4	
ID12B	Source-DFM distance	28 m
	Grazing angle on DFM and HFM	2°
	Source-HFM distance	29.5 m
	HFM-exit slit distance	ca. 20.5 m
	HFM geometrical magnification factor	0.7
	Source-VFM distance	36.5 m
	VFM-spherical grating entrance slit distance	7.55 m
	VFM geometrical magnification factor	0.21
	Grazing angle on VFM and PFM	1.45°
	Beam footprint on VFM	120 mm = L/2.1
	Beam footprint on PFM	15 mm = L/3.3
	Source-Spherical grating distance	46.05 m
	Source-PFM distance	54.56 m
	distance spherical grating exit slit-PFM	ca. 4.5 m
	distance PFM-sample	ca. 1 m
	PFM-magnification factor	ca. 0.2
	Coating (all mirrors)	Pt
DFM, HFM & VFM dimensions (length (L), width, thickness)	250 x 50 x 20 mm ³	
PFM dimensions (length (L), width, thickness)	50 x 30 x 20 mm ³	
Roughness rms (all mirrors)	< 4 Å	

3. MIRROR METROLOGY

3.1. Data reduction

Accurate measurements of the mirror profiles were carried out using the Linear Trace Profiler^{10,11} (LTP) of the ESRF metrology laboratory. The ESRF LTP design comes from the original work of P. Takacs at the Brookhaven National Laboratory.¹² It is based on a two beam Michelson interferometer and provides absolute 2D slope data for a longitudinal trace along the mirror that is being measured. A laser beam is split into two components forming an interference pattern and is scanned along the mirror (min. step 0.5 mm, probe size 2.0 mm, max scanned length 2 m). After reflection from the surface being tested, the fringe intensity pattern is focused onto a 1024 element Si photodiode array detector. Its position on the latter is directly related to the slope on the mirror surface. Slope errors measurements with resolution better than 1 μrad in the tangential direction over spatial wavelengths from a few mm to nearly the length of the tested optical element are routinely achieved. For all the measurements of the VF-2M mirrors, the stability and repeatability of the benders was found to be of the order of magnitude of the LTP noise: 0.5 microradians (equivalent to 8 nanometers on a 1000 mm long flat mirror) rms for dynamic precision and 0.8 microradians (equivalent to 17 nanometers on a 500 mm long flat mirror) rms for accuracy. ID12B mirrors have a fixed bending radius, so that a single trace is enough to characterize each of them.

The slope raw data from the LTP ($\alpha_{raw}(x_i)$, $i = 1, \dots, N$, with N the number of measuring points) are first linearly fitted to a straight line $\alpha_{fit}(x_i) = Ax_i + B$. The spherical radius is given by the reciprocal of the straight line slope ($R = 1/A$). The figure slope error ($\alpha(x_i)$) is obtained by subtracting the best fit straight line from the raw slope data $\alpha(x_i) = \alpha_{raw}(x_i) - \alpha_{fit}(x_i)$. This process is called linear detrending. Finally, the slope error mapping is integrated to give the height error profile $z(x_i)$. The integration is done with 5-point Newton-Cotes routine that approximates numerically the formula:

$$z(x_i) = \int_{x_1}^{x_i} \alpha(y) dy. \quad (1)$$

The slope error rms is given by the following definition:

$$\sigma_{rms} = \sqrt{\frac{1}{N} \sum_{i=1}^N (\alpha(x_i))^2}. \quad (2)$$

The value of rms slope error is definitely not enough to fully characterize the surface. The figure, waviness and roughness frequencies included in the measured profile are evidenced when calculating the Fourier transform of the profile. The Fourier transform is peaked at frequencies corresponding to characteristic lengths that do show in the profile. The power-spectral-density function (PSD) is the frequency spectrum of the surface profile measured in inverse length units and is basically proportional to the square modulus of its Fourier transform. It can be calculated numerically using Ref. 13:

$$S(f_m) = \frac{2D}{N} \left| \sum_{i=1}^N e^{-2\pi i(m-1)(n-1)/N} W(x_n) z(x_n) \right|^2 \quad (3)$$

where W is a weighting window (we used a Hanning window) to avoid border effects, and $D = x_n - x_{n-1}$ is the sampling distance. The positions of the peaks in the PSD function give the period of the oscillations included in the profile. The type of information (figure, waviness or roughness) that the PSD contains, or in other words the frequency domain, depends on the length (L) and sampling step (D) of the profile. The lowest (fundamental) frequency is given by the reciprocal ($1/L$) of the sampled length and is associated to the longest spatial period. The frequency spacing is equal to this lowest component ($1/L$). The frequency upper limit is given by the foldover (also called 'Nyquist') frequency, defined as $1/2D$ or equivalently as $N/2L$. The reciprocal of the Nyquist frequency determines the shortest spatial period included in the data set (corresponding to the distance between point x_i and point x_{i+2}).

3.2. Mirrors measurements

The two mirrors of the ID12A beamline VF-2M device were measured in the LTP for 10 different piezo elongations, which correspond to equally spaced points in the variable $1/R$, R being the curvature radius. The height errors from the best fit sphere (detrended height) are shown in Fig. 2. Slope errors rms and other parameters related to these profiles are reported in Fig. 3. It is worth noting that the detrended height profiles are highly structured. If one approximates, in first order, the Fig. 2 profiles with a pure sinusoid, such a function would have a characteristic spatial period of the order of $L/2$, L being the mirror length. It is clear that these low-frequency deformations will appreciably affect the focused image.

Six ID12B beamline mirrors were measured in the metrology laboratory: DFM1,DFM2,HFM1,HFM2,VFM and PFM. The measured slope errors for these mirrors are 3.6, 2.9, 5.0, 2.55, 1.99, 1.0 μrad rms respectively. The best fit spherical radii for the HFM1 and HFM2 were 945.0 and 912.2 m, respectively. For the VFM and PFM the measured radii are 508.3 m and 61.7 m, respectively. The height profiles corresponding to the ones used in the Shadow simulations can be found in Fig. 4.

All ID12B mirrors still show a "wavy" detrended height profile. The mirrors deflecting/focusing the beam in the horizontal plane (DFMs and HFMs) show wider amplitude oscillations, but their effect on the final image is completely smeared by the convolution with the contribution due to the relatively large horizontal source size. On the other hand, mirrors operating in the vertical plane (VFM and PFM) are much more sensitive to waviness, as the contribution due to source size is at least one order of magnitude smaller. This is the reason for their tighter polishing specifications, which lead to much less structured profiles.

Two additional profiles were measured on the VFM to check its isotropy in the transversal direction. These LTP scans are close to the mirror edges (15 mm apart from the central profile). The results of these measurements are: slope error 2.97 and 2.11 (central 1.99) $\mu rads$ rms and best radii fit 508.4 and 505.9 (central 508.3) meters.

4. RAY-TRACING RESULTS

4.1. Introduction

The ray-tracing method is a simulation technique that allows computer experiments to be performed with a given optical system. We used the SHADOW code to carry out our calculations. SHADOW first creates a set of rays in a

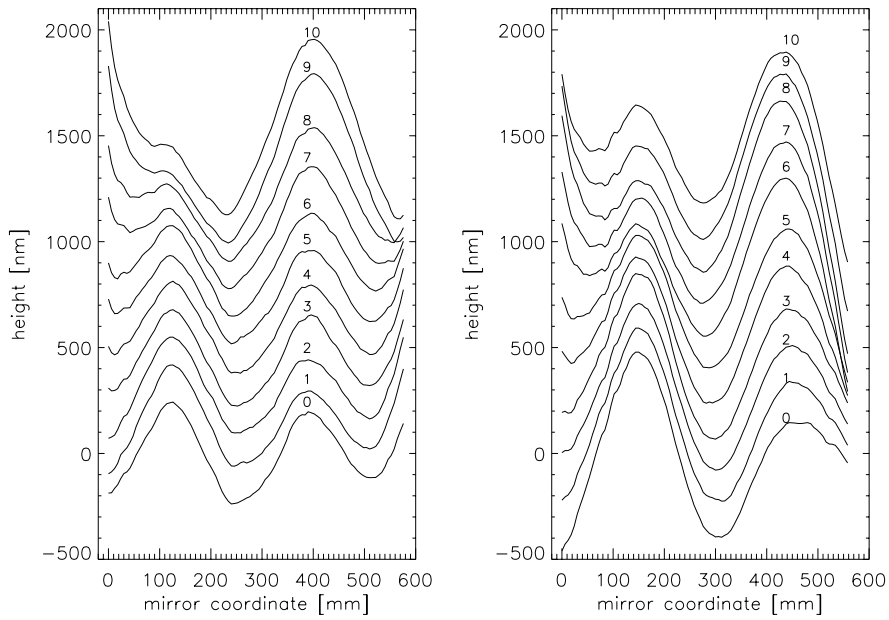


Figure 2. Detrended height profiles for ID12A M1 (left) and M2 (right). Different profiles correspond to bender scans to reach curvatures from +1 Km (profile 0) to -1 Km (profile 10). Profiles from 1 to 10 have been shifted by 150 nm in Y axis for clarity.

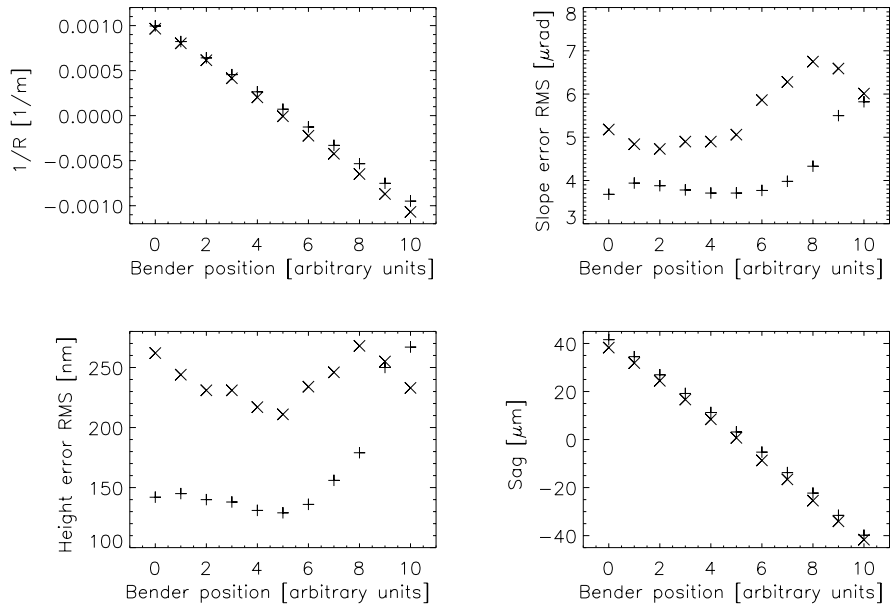


Figure 3. Curvature radii, slope error rms, height error rms and mirror sag of ID12A M1 (+) and M2 (x), as a function of the bender scanning parameter. Each bender scanning value corresponds to a profile in Fig. 2.

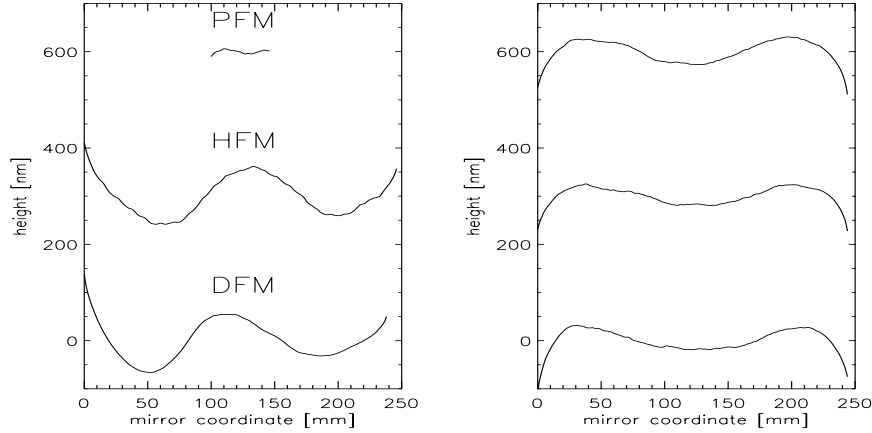


Figure 4. Detrended height profiles for ID12B mirrors. Left: DFM, HFM and PFM profiles. Right: Three profiles measured from the VFM. Some profiles were shifted by 300 nm in Y-axis for better clarity.

Table 2. Effective source dimensions (FWHM) in real space (x, z) and divergence space (x', z') from SHADOW.

	ID12A	ID12B
x	725 μm	760 μm
z	37 μm	20 μm
x'	33.6 μrad	60.7 μrad
z'	28.9 μrad	70.1 μrad

given region of the phase space (the source). Each ray is fully described by four vectors and two phases: the starting position \vec{r} , the wavevector \vec{k} , the electric vectors \vec{A}_s and \vec{A}_p and their associated phases ϕ_s and ϕ_p . The source rays are generated using the Monte Carlo technique to sample the spatial, angular and spectral distributions of the synchrotron sources (an undulator in our case). Each ray is then traced through an optical system consisting of a freely variable number of optical elements (mirrors/monochromators...). The mirrors surface may have any mathematical shape (ellipsoidal, spherical, etc). It is also possible to add to this ideal surface a mesh surface of imperfections. This feature allows to evaluate the effect of slope errors (measured or modelled), thermal deformations (calculated theoretically or by finite elements), gravity sag and/or any other figure error. We were interested in calculating the spot dimensions and its degradation due to the slope error effects. To accomplish this task, we calculated the ray distribution at the focal position.

To include the measured interferometric profiles in SHADOW, we used its PRESURFACE module, which can accept a numerical mesh for a surface. This surface spline is added to the main mathematically defined profile (spherical, cylindrical, etc.). We built such numerical surfaces by replicating transversally each profile obtained from the metrology measurements.

The sources for the calculation are the Helios I & II undulators tuned to shift the first harmonic peak at energies of ca. 0.8 and 5 KeV for ID12B and ID12A, respectively. The effective source dimensions, computed by SHADOW from the storage ring and insertion device parameters are summarized in table 2. Beamline monochromators are set to operate at these energies. Several simulations were carried out using the different available profiles. We only present the simulations corresponding to the cases when experimental measurements of the focal intensity distribution are available for reference and comparison.

4.2. ID12A

Ray-tracing runs using available height error profiles of ID12A mirrors give essentially the same results, as can be deduced by looking at the similarity of the profiles (see Fig. 2). We then choose to investigate more in detail the optical setup experimentally tested on the beamline. The focusing configuration of the VF-2M is obtained by first

aligning and bending M1 (keeping M2 flat) until obtaining its best focal spot and then M2 is also bent to improve the focal spot. The experimental data points were recorded by scanning the beam reflected by M2 over a slit of $52 \mu\text{m}$ aperture (M2 angular scan width: ca. $50 \mu\text{rad}$): the transmitted intensity as a function of the mirror angular position was recorded by means of a silicon photodiode detector operated in photoconductive mode. The raw data were then deconvoluted to take into account the slit size. By using a calibration table derived from the LTP measurements, it is possible to associate with each bender voltage readout a best fit spherical curvature (see Fig. 3). These bending radii (4809 m concave for M1 and 154232 m convex for M2) were included in SHADOW to define the main cylindrical curvature. The simulation results for three cases (no slope error, slope error from measured profiles and slope errors calculated with the method in Ref. 14) are shown in Fig. 5.

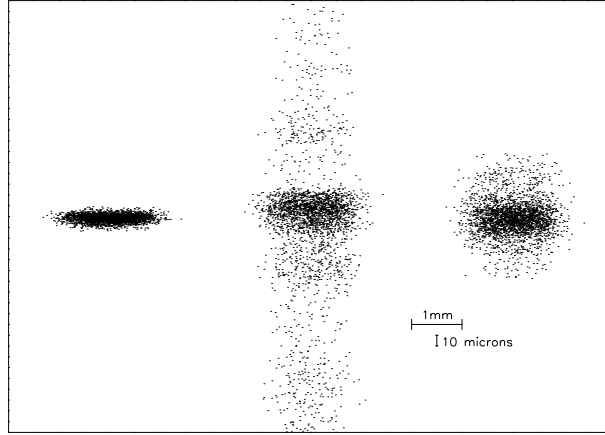


Figure 5. Ray-tracing simulation of VF-2M experimental focusing configuration for three cases: no slope error (left), slope error from LTP measurements (center) and slope error (ca. 1.15 arcsec on both mirrors) with model in Ref. 14 (right). The vertical FWHM values are 8, 24 and 26 μm , respectively. There is no focusing in the horizontal plane. Note the structures associated with the measured figure slope errors (central spot).

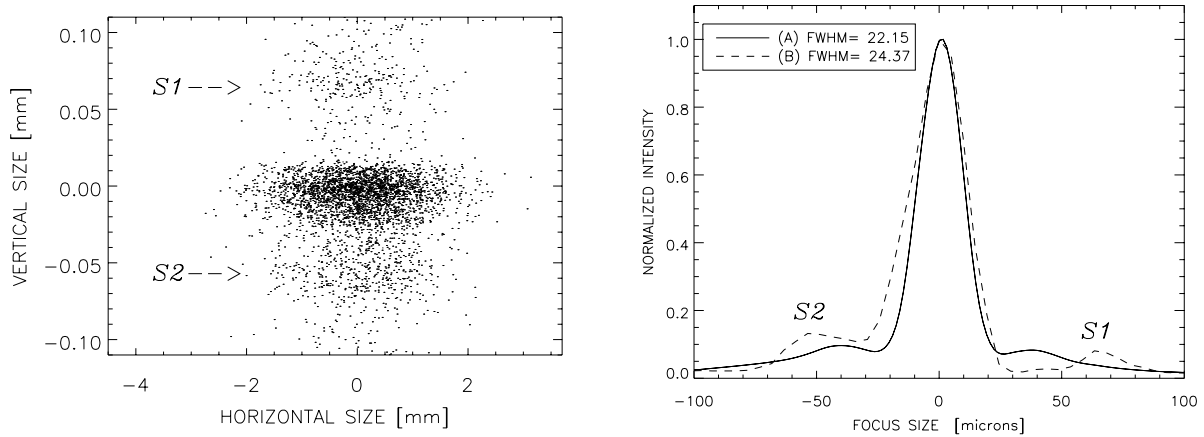


Figure 6. Left: SHADOW calculation for VF-2M focal spot (same as in Fig. 5 (center)). Right: Superposition of the experimental (A) and calculated (B) vertical intensity profile at the ID12A VF-2M focal position. The satellite structures $S1$ and $S2$, which are due to the mirror slope error are evident in both curves.

The spot obtained using the real slope errors exhibits two satellite structures in the vertical direction that are also present in the real beamline spot, as shown in Fig. 6. The good agreement between experimental and simulated data is evident from this figure. It is worth to stress here that the satellite structures $S1$ and $S2$ are intrinsic to the

mirrors surfaces themselves and it is not possible to get rid of them by a better alignment. The only way to reduce or remove them is to limit the beam footprint on the mirror itself, thus lowering the vertical angular acceptance. This solution is not always acceptable because it reduces considerably the flux at the sample position.

We also investigated the dependence of the focal spot position and size from the reflecting surface PSD. The comparison between the simulated FWHM vertical spot size obtained from the real mirrors with the one calculated for their ideal counterparts (M1 and M2 bent to the ideal spherical radii mentioned above) gives similar numbers: 24 μm for the first and 17 μm for the latter. However, we found a dramatic change in the M2 to focal spot distance: in the first case the VF-2M focuses at 7.64 m ("experimental focus") but when we remove the surface error spline this distance increases dramatically by 9.5 m, up to 17.14 m ("ideal sphere focus")! We claim that this anomalous behaviour is totally due to the specific M1 and M2 detrended height profiles. We demonstrated our assumption by two different methods, reported hereafter.

The wavy profiles reported in Fig. 2 exhibit a periodicity of ca. $L/2$ and the "valley-like" structure present in the mirrors central portion clearly alters locally the curvature seen by the impinging photon beam (effective spherical radius: R_{eff}). As the main (baseline) spherical radius (R_{LTPfit}) has already been subtracted from the Fig. 2 profiles, this sinusoidal polishing error generates an additional concave curvature (R_{pol}) that adds up to the LTP best fit radius. R_{pol} , R_{LTPfit} and R_{eff} are related according to the following formula:

$$\frac{1}{R_{eff}} = \frac{1}{R_{LTPfit}} + \frac{1}{R_{pol}} \quad (4)$$

R_{pol} is approx. 15 Km for both M1 and M2, so that by adding up the LTP best fit radii (M1 = 4809 m, M2 = -154232 m) as in eq. 4, one finds shorter effective radii of the order of 3.5 and 15 Km for M1 and M2, respectively. It is worth noting that the sign of M2 radius is reversed, thus indicating a shift from convex to concave shape! The final step was to carry out a SHADOW run using ideally spherical profiles for M1 and M2 (with the above mentioned effective radii) to determine the new position of the "ideal sphere focus". This time it turned out to be almost coincident (within 20 cm) with the "experimental focus", 7.64 m after M2.

The second method to understand the origin of the focal spot 9.5 m downstream shift, consists in studying the effect of a progressive filtering out of the lower frequency components in the detrended height curves. By applying an ideal high pass filter, we selectively attenuated all the frequencies lower than a given ν_{limit} in Fig. 2 profiles. We let ν_{limit} vary between $1/L$ and $24/L \text{ mm}^{-1}$. The resulting filtered detrended height curves (see Fig. 7 and Fig. 8 top) were then inserted in SHADOW. The evolution of the "experimental focus" and of the "ideal sphere focus" was characterized by defining two fixed position screens, situated at 7.64 and 17.14 m after M2. Starting from the unfiltered profile, almost nothing happens for $\nu_{limit} < 2/L$: the beam is still focalized at 7.64 m after M2 and is totally defocused at the second screen position. As soon as $\nu_{limit} \geq 2/L$ the situation is reversed: no more focusing is detected on the first screen and the beam starts focusing at the "ideal sphere focus" position. Structures in the focalized beam due to waviness are still clearly visible on the second screen and also in the beam vertical section at the "experimental focus" location. Increasing ν_{limit} reduces the beam FWHM vertical size at 17.14 m from M2 and, moreover, gradually eliminates the waviness structure. Eventually, when $\nu_{limit} \geq 24/L$, the FWHM reaches the lower limit value of 17 μm and no structures are present any more. This calculation points out once again the importance of the low end of the PSD in determining the focusing properties of a grazing incidence mirror and the effect of the low/mid-range frequencies in creating structures in the reflected beam.

4.3. ID12B

We carried out ray-tracing simulations on the two vertically focusing mirrors (VFM and PFM), as they are, together with the spherical grating, the most crucial optical elements of the beamline. Their smoother (if compared to the VF-2M ones) detrended height profiles do not generate artifacts such as small satellites in the focal spot; nevertheless a non-negligible broadening (a factor of about 2) of the final image due to mid-frequency errors is clearly present. The smaller waviness amplitude leads to a better agreement between the best fit spherical radius and the effective focusing properties. Small ($\pm 3\%$) adjustments of the nominal incidence angle are still needed to minimize the beam vertical dimension at a given position (slits/sample), but even if no angular correction is applied, the experimental least confusion circle falls always within a few centimeters from the theoretical one (typically 2-3% downstream of the ideal focusing distance for the VFM). Results are shown in Fig. 9.

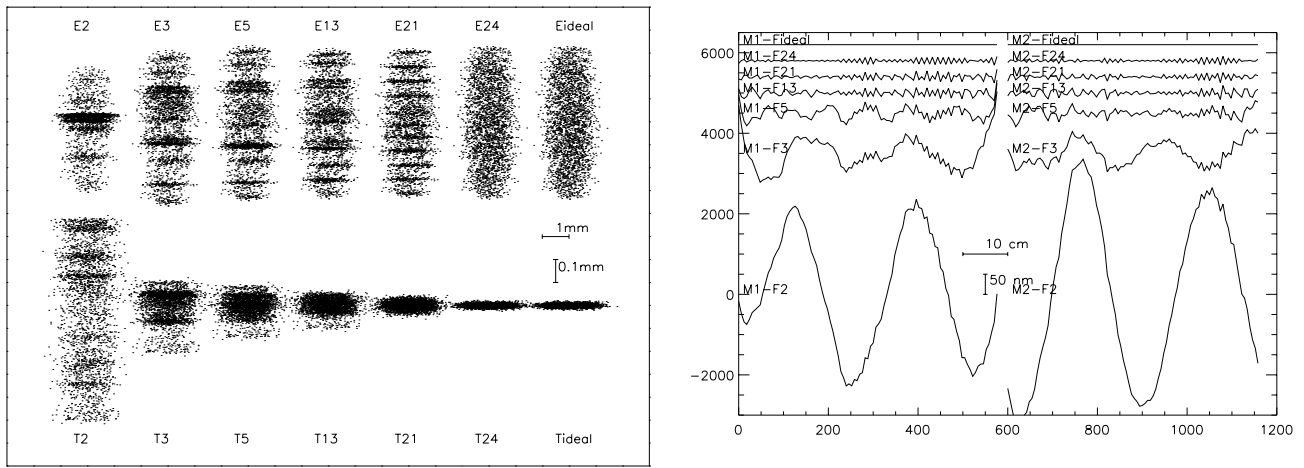


Figure 7. Left: Calculated spot shapes with Fourier filtered profiles for M1 and M2. The spot size is shown in two position: at the experimental location 7.62 m from M2 (labeled E_n) and at the theoretical focus location at 17.14 m from M2 (labelled T_n). The n value means that the applied cutoff frequency is n/L . Right: the corresponding filtered profiles for M1 and M2. Filtered values are labelled with F_n , with the described meaning for n . E/T/Fideal stands for ideally spherical mirrors.

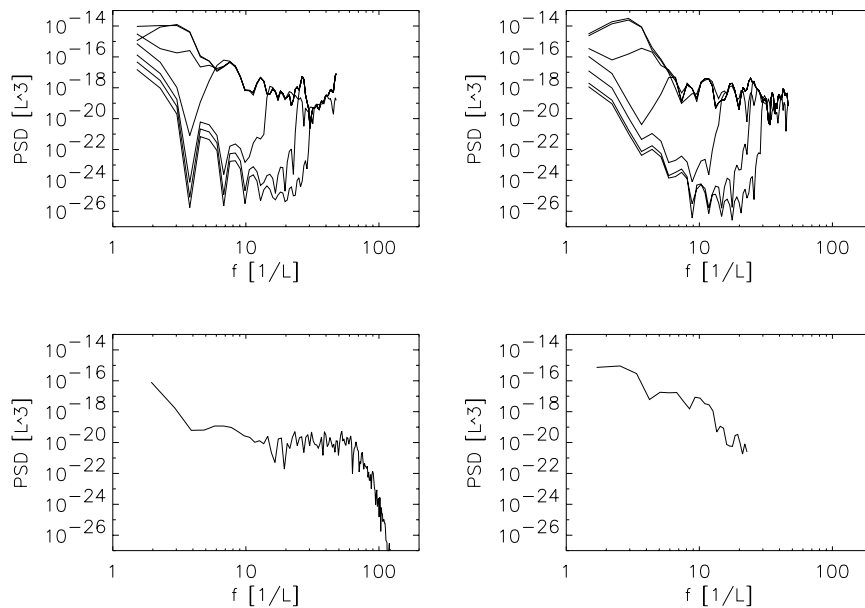


Figure 8. Top: Effect of progressive Fourier filtering on the PSD functions for ID12A mirrors M1 (left) and M2(right). The higher curve corresponds to the PSD of the non-filtered profile. The other six curves refer to the filtered profiles shown in Fig. 7 (cutoff frequencies: $2/L$, $3/L$, $5/L$, $13/L$, $21/L$ and $24/L$, respectively). Bottom: PSD for ID12B VFM (left) and PFM (right). Note that the low frequencies are enhanced in the non-filtered ID12A mirrors respect to the ID12B ones. These peaks in the low frequency range are responsible for the focal spot structures (see text).

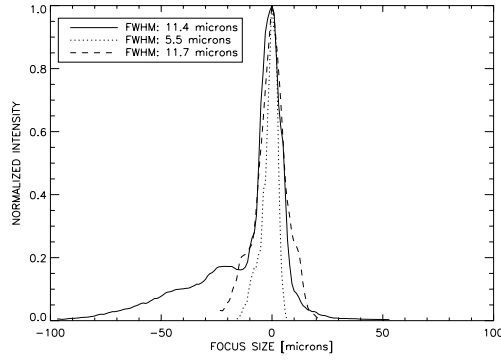


Figure 9. Solid line: Experimental vertical spot produced by the ID12B VFM. Dotted line: calculated spot profile when no slope errors are taken into account. Dashed line: calculated spot with slope errors from the measured profile.

The most evident feature in the calculated VFM focal spot is the optical aberrations asymmetrical tail, which is also present in the experimental data. This tail is clearly visible in the calculated spot profile obtained with an ideal spherical shape for the VFM. It is partially washed out by the convolution with the broadening due to waviness effects. The huge asymmetry of the experimental data profile can be explained only partially by blurring due to optical aberrations. Probably, other non-optical effects are spoiling the VFM focus size (... masks partially cutting out the beam ?) and accurate measurements are planned after beamline realignment.

We also validated the hypothesis advanced by beamline staff that the VFM surface is not strictly isotropic: different spot sizes are obtained as a function of the footprint position. The three different profiles reported in Fig. 4 (right) give respectively 9,12 and 14 μm for the calculated FWHM vertical spot size. By averaging out these data we end up with a result that agrees remarkably well with the experimental one (11.4 μm FWHM). Finally, we came to the conclusion that the ideal (without slope errors) FWHM vertical spot size (approx. 5.5 μm) is not reachable with the actual VFM and then no beamtime should be dedicated to improving experimentally the optical setup positioning (except for the tail origin problem) to obtain a smaller focus size.

We do not report here on SHADOW simulations for the PFM, as we ended up with the conclusion that a more sophisticated procedure is needed to take the experimental data. As a matter of fact, ray-tracing indicates a FWHM value which is ca. a factor of two smaller than the beamline measurements, but this is probably due to the lack of sufficient resolution on the movement needed to scan the focused beam over the measuring slit. Moreover the slit is clearly oversized for a few microns range measurements. To cope with this problem a much smaller, calibrated slit will be installed during the next Summer shutdown, thus allowing a much better quality for the experimental focus size data.

5. CONCLUSION

Ray-tracing calculations using measured mirror profiles give final images showing structures which are absent when perfectly spherical (or aspherical) surfaces are considered. The origin of these artifacts in the final image is directly related to the mirror reflecting surface texture. We calculated several PSDs from the different mirrors profiles that we inserted in the ray-tracing code SHADOW. These functions are shown in Fig. 8. All length units are normalized to the mirror length (L), thus one finds in the abscissas axes the frequencies corresponding to multiples of the fundamental frequency $1/L \text{ mm}^{-1}$. An important plateau (absent in the ID12B mirrors PSDs) in the low frequency range is easily recognized for ID12A mirrors PSDs. These low frequency components are clearly responsible for the overfocusing effect observed experimentally on ID12A. They also generate, together with slightly higher frequencies, satellite structures visible in the ray-tracing results as well as in the experimental data. In the spot profiles measured and calculated for beamline ID12B, these structures do not appear (see Fig. 9). It can be noticed from Fig. 4, that this beamline mirrors present less structured detrended heights, specially in the VFM and PFM case, the mirrors

that perform the vertical focusing of the beam. It has been shown that surfaces containing frequencies higher than $15/L$ do not produce satellite structures for our particular cases.

A numerical method for including ab-initio simulated slope errors¹⁴ has been tested (see Fig. 5). It is clear that any ab-initio method based only on rms slope error values will fail in simulating the artifacts found in the experimental data, as the PSD alone does not contain all the information needed to unequivocally determine the position and intensity of the satellites. Polishing errors enhancing the PSD low frequency region should be carefully avoided (with the exception of multi-segmented bimorph mirrors¹⁵), but peaks in that zone do not always produce satellite structures if the structural errors are located in a non-critical area of the mirror.

We strongly recommend to write "PSD-based" specifications¹⁶ for x-ray mirrors optical polishing, keeping in mind that accurate post-delivery metrology and ray-tracing using the measured real profiles can be extremely helpful to commission beamline optics.

ACKNOWLEDGEMENTS

The authors wish to thank Dr José Goulon, beamline responsible for ID12A and ESRF EXAFS group leader, and the ID12A staff for support in the VF-2M design, assembly, installation and commissioning. Dr Nicholas Brookes, beamline responsible for ID12B, and the ID12B beamline staff for supplying the VFM and PFM experimental data and (Dr. Brookes) for proof-reading the manuscript and many fruitful discussions.

REFERENCES

1. C. Welnak, G-J Chen and F. Cerrina, "SHADOW: a synchrotron radiation and x-ray optics simulation tool," *Nucl. Instr. Meth.* **A347**, pp. 344-347, 1994.
2. H. Dagnall M.A., *Exploring surface texture*, Rank Taylor Hobson, Leicester, 1986.
3. P. Elleaume, "Helios: a new type of linear/helical undulator," *Journal of Synchrotron Radiation* **1**, pp. 19-26, 1994.
4. P. Elleaume, J. Chavanne, X. Marechal, J. Goulon, L. Braicovich, C. Malgrange, H. Emerich, G. Marot and J. Susini, "An Esrf beamline dedicated to polarization sensitive XAS at low excitation energies," *Nucl. Instr. and Meth.* **A308**, pp. 382-389, 1991.
5. J. Goulon, N.B. Brookes, C. Gauthier, J. Goedkoop, C. Goulon-Ginet, M. Hagelstein and A. Rogalev, "Instrumentation development for Esrf beamlines," *Physica B* **208/209**, pp. 199-202, 1995.
6. R. Signorato, C. Goulon-Ginet, J. Goulon, A. Rogalev, J-J Fermé, "Vertically focusing reflective optics using two bendable CVD SiC mirrors," in *Optics for high brightness synchrotron radiation II, Proc. SPIE* **2856**, 1996.
7. R. Signorato, C. Goulon-Ginet, J. Goulon, A. Rogalev, P. Marion and J-J Fermé, "Vertically focusing double mirror device (VF-2M) for the ESRF beamline ID12A," in *Proceedings of XAFS IX conference*, Les éditions de physique, ed., *J. phys IV France* **71**, pp. C2-341/342, 1997.
8. C. T. Chen, "Concept and design procedure for cylindrical element monochromators for synchrotron radiation," *Nucl. Instr. and Meth.* **A256**, pp. 595-604, 1987.
9. C. T. Chen and F. Sette, "Performance of the Dragon soft x-ray beamline," *Rev. Sci. Instrum.* **60(7)**, pp. 1616-1621, 1989.
10. J. Susini, R. Baker and A. Vivo, "Optical metrology facility at the ESRF," *Rev. Sci. Instrum.* **66**, pp. 2232-2234, 1995.
11. O. Hignette and A. Rommeveaux, "Status of the optical metrology at the ESRF," in *Optics for high brightness synchrotron radiation II, Proc. SPIE* **2856**, p. 315, 1996.
12. P. Takacs, "Design of a LTP; metrology figure and finish," *Proc. SPIE* **749**, p. 59, 1987.
13. E. L. Church and P. Takacs, "Use of an optical profiling instrument for the measurement of the figure and finish of optical quality surfaces," *Wear* **109**, pp. 241-257, 1986.
14. M. Sanchez del Rio and A. Marcelli, "Waviness effects in Ray-tracing of 'real' optical surfaces," *Nucl. Instr. and Meth.* **A319**, pp. 170-177, 1992.
15. R. Signorato et al., "Multi-segmented piezoelectric bimorph mirrors as active/adaptive optics components," *Proc. SRI97*, in preparation-to be published in 1998.
16. R. Signorato, *Technical specifications for the ESRF beamline ID26 Vertically Focusing Mirror 3 optical polishing by SESO Inc.*, 1997.